Su, Z., Yoon, J. S., Zang, A., Tang, L., Gu, H., Zhu, C. (2021): Stress Reorientation by Earthquakes Near the Ganzi-Yushu Strike-Slip Fault and Interpretation with Discrete Element Modelling. - Rock Mechanics and Rock Engineering, 54, 5433-5447.

https://doi.org/10.1007/s00603-021-02443-w

Stress Reorientation by Earthquakes near the Ganzi-Yushu Strike-Slip Fault and Interpretation with Discrete Element Modelling

Zhandong Su[1,2], Jeoung Seok Yoon[3], Arno Zang[4], Lei Tang[5], Hongbiao Gu[1], Chuanbing Zhu[4]

1 Institute of Disaster Prevention, China Earthquake Administration, Sanhe, China, 065201

2 Hebei Key Laboratory of Earthquake Disaster Prevention and Risk Assessment, Sanhe, China, 065201

3 DynaFrax UG (limited liability company), Potsdam, Germany, 14467

4 Section 2.6 Seismic Hazard and Risk Dynamics, GFZ—German Research Centre for Geosciences, Telegrafenberg, Potsdam, Germany, 14473

5 Institute of Crustal Dynamics, China Earthquake Administration, Beijing, China, 100085

Abstract

Earthquakes are generally known to alter the stress field near seismogenic faults. Observations using YRY-four-gauge borehole strainmeters within Yushu (YSH) borehole near the Ganzi-Yushu fault in eastern Tibetan Plateau shows that the azimuth variation of maximum horizontal stress (S_{H}) first decreased and then increased substantially when the earthquakes occurred during the measurement period from January 1, 2009 to December 31, 2018. In this period, 38 earthquakes (M ≥3) were detected near the fault and the S_{H} orientation showed a drastic change after the 2010 *M*s 7.3 Yushu mainshock. We present a discrete element modelling using Particle Flow Code 2D (PFC2D) to simulate a dynamic fault rupturing process and to use the modelling results for interpretation of the stress reorientation. The modelling reveals that dilatation and compression quadrants are formed around a fault rupturing in strike-slip model, resulting in different spatiotemporal changes of the orientation of maximum horizontal stress ($\Delta\theta$). The value of $\Delta\theta$ in the compression quadrants shows a sharp drop at the time of coseismic slip, then approaches slowly to an asymptotic value. In the dilatation quadrants, $\Delta\theta$ drops by coseismic slip, then increases sharply and finally reaches a stable value. The modelled $\Delta\theta$ by coseismic fault slip agrees with in-situ observations at YSH borehole during 2010 *M*s 7.3 Yushu mainshock. It is also found that, the value of $\Delta\theta$ decreases with increasing distance from the rupturing source. We modelled the effect of fault geometry and host rock properties on the

$\Delta\theta$, and found that structural complexity and off-fault damage by coseismic fault slip have significant impact on the stress field alteration near the rupturing source.

Keywords Yushu earthquakes; Ganzi-Yushu strike-slip fault; Stress reorientation; Discrete Element Modeling; Dilatation and compression stress quadrants

List of Symbols

M	Magnitude of earthquakes
Mw	Moment magnitude of earthquakes
M_L	Local magnitude of earthquakes
M_S	Surface-wave magnitude of earthquakes
S_h	Minimum horizontal principal stress
S_H	Maximum horizontal principal stress
$\Delta\theta$	Change of the orientation of maximum horizontal stress
SAF	San Andreas Fault
FGBS	Four-gauge borehole strainmeter
φ	Principal strain orientation
ε_1	First strain reading of FGBS
ε_2	Second strain reading of FGBS
ε_3	Third strain reading of FGBS
ε_4	Fourth strain reading of FGBS
θ_1	Azimuth of ε_1 gauge
YSH	Yushu
YRY	Ya Rong Yi

LE	Linear fault with elastic rock mass
LEP	Linear fault with elasto-plastic rock mass
CE	Curved fault with elastic rock mass
CEP	Curved fault with elasto-plastic rock mass
DEM	Distinct element method
$\Delta\alpha$	Rotation angle
δ	Stress ratio
σ_{xx}	Maximum normal stress
σ_{yy}	Minimum normal stress
τ_{xy}	Shear stress

1 Introduction

The state of the crustal stress field is of great importance for our understanding of the stability of underground excavations, geodynamic processes, and seismic hazard assessment (Fuchs and Muller 2001; Hu et al. 2017; Stephansson and Zang 2012; Zang and Stephansson 2010). Stress and earthquakes are generally known to be interrelated; that is, stress triggers earthquakes and earthquakes, in turn, alter the stress state on surrounding faults (Agnès et al. 2005; Hardebeck 2004; Harris 1998; Kilb et al. 2000; Lin et al. 2007; Reasenberg and Simpson 1992; Stein et al. 2010; Stein 2000). The earthquake-induced stress changes, i.e., stress rotations, are commonly used in characterizing the evolution of post-seismic stress and understanding the earthquake-stress interaction and the reloading of faults (Hardebeck and Okada 2018).

The rotation of the S_H has been investigated based on the inversion of focal mechanisms along the strike-slip fault ruptures. For instance, Hauksson (1994) concluded that S_H rotated 5°-24° clockwise during the M_w 6.1 Joshua Tree earthquake and flipped back to the pre-Joshua Tree orientation state when the M_w 7.3 Landers mainshock occurred. Zhao et al. (1997) derived a counterclockwise rotation of principal stress axis of ca. 20° at the time of the M_w 6.7 Northridge earthquake and a slow return to the original state. Ratchkovski (2003) demonstrated that the principal stress axis rotated ~20° in the vicinity of the 2002 M_w 7.9 earthquake mainshock hypocenter relative to the strike-slip Denali fault. Bohnhoff (2006) investigated the stress reorientation due to the 1999 Mw 7.4 Izmit main earthquake and the aftershock along the right-lateral slip striking EW using 446 fault plane solutions. He concluded that the maximum horizontal compressive stress axis rotated anti-clockwise 8° in the Izmit-Sapanca area whereas it rotated clockwise towards the eastern end of the rupture. Yoshida et al. (2014) have investigated the stress field regarding the 2008 *M* 7.2 Iwate-Miyagi Nairiku earthquake in NE Japan, and found the maximum principal stress axes differ remarkably before and after the main shock. Stress rotations were also examined during the 2016 *M* 7.3 Kumamoto earthquake along the Futagawa-Hinagu fault zone, that is, the minimum principal stress axes in the vicinity of the fault plane significantly rotated counterclockwise after the *M* 6.5 foreshock and rotated clockwise after the *M* 7.3 main shock in the Hinagu fault segment (Yoshida et al., 2016b; Yu et al., 2019). However, the stress changes based on focal mechanism inversion along strike-slip faults are predominately shown as an overall pattern irrespective of individual stress variation related to fault segments.

In-situ stress measurements provide also information on stress reorientation pattern from the upper plate. It is known that localized stress rotations measured and detected in the vicinity of faults penetrated by boreholes reveal that this reorientation phenomenon is associated with the slip motion of pre-existing active faults (Barton and Zoback 1994; Kerkela and Stock 1996; Paillet and Kim 1987; Shamir and Zoback 1992). The orientation of S_H measured far away from the San Andreas Fault (SAF) is NNE. However, the azimuth of the S_H measured near the fault approximately rotates to EW or NW (Sbar et al. 1979), perpendicular to the strike of the SAF in its immediate vicinity. Such spatial variations were also observed to be markedly associated with plate movement (Fuchs and Muller 2001). However, the stress rotations observed locally at several wellbores were presented, and fewer efforts have been made tracing the dynamic variation of S_H within or near the borehole, and investigating the overall stress reorientation pattern along a segmented strike-slip fault.

Hence, our study objective is mainly focused on the temporal and spatial variation patterns of S_H along the Ganzi-Yushu strike-slip fault during earthquake occurrence and understanding the physics behind this phenomenon by numerical modeling. A systematic investigation of the impact of fault geometry (linear fault and curved-segmented fault) and rock properties (elastic and elasto-plastic) on the spatiotemporal changes in the stress orientation around the Ganzi-Yushu fault rupture is performed numerically.

2 Tectonic setting

The study region is located in a high mountain region along the Ganzi-Yushu fault zone in central-eastern Tibet, China (Fig. 1). The Ganzi-Yushu Fault is part of the Xianshuihe Fault system (Shifeng et al. 2008). Based on the inversion of the seismic focal mechanism, the Ganzi-Yushu fault zone exhibits approximately left-lateral slip on a sub-vertical plane striking WNW-ESE. This is in response to the eastward extrusion and northeastward shortening of the central Tibetan Plateau due to the continuing collision of the Indian Plate and the Eurasian Plate. On April 14, 2010, an Mw 6.9 earthquake occurred on the Ganzi-Yushu fault and resulted in widespread damage (Tobita et al. 2011). There are 38 aftershocks with M >3 which occurred within the study region including seven aftershocks with M >4.8 (Table 1 and Fig. 1b). Field investigations show that the Yushu earthquake produced a surface rupture zone more than 30 km long with a maximum left-lateral displacement of 3.2 meter in the central part of the Yushu rupture (Lin et al. 2011b). In 1738, an M 7.5 event located in the vicinity of the 2010 event is reported (Lin et al. 2011a). Along the Ganzi-Yushu fault, the total average left-lateral slip-rate has been estimated to be more than 10 mm/a (Wang et al. 2001; Wen et al. 2003). The slip deformation and seismicity data show that the Ganzi-Yushu fault zone is currently active as a seismogenic fault that triggers large-magnitude earthquakes.

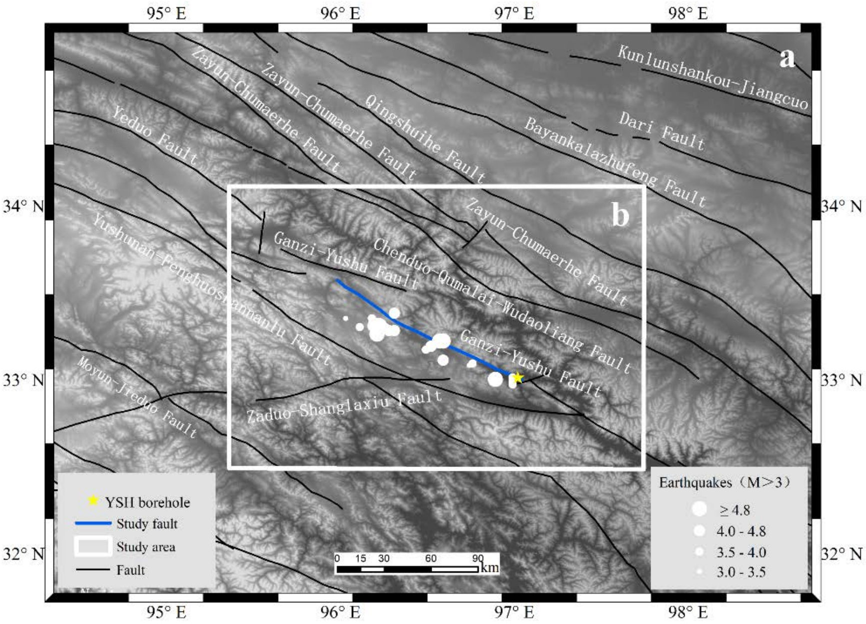

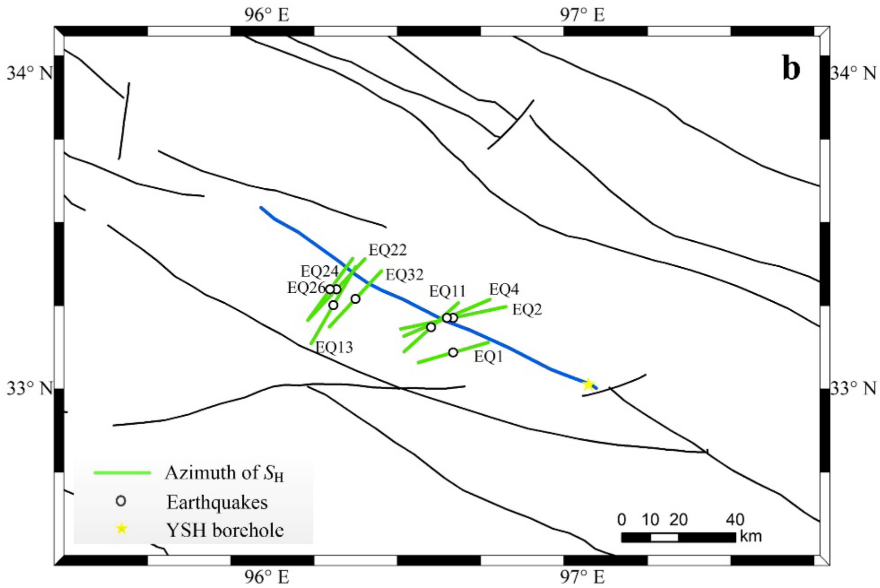

Fig. 1 (a) Color-shaded relief map modified from GDEMDEM 30m data (the data set is provided by Geospatial Data Cloud site, Computer Network Information Center, Chinese Academy of Sciences) showing the topographic and tectonic setting of the study area (white rectangle). The blue solid line denotes the study fault (Ganzi-Yushu fault) and the black solid lines denote the faults near the study fault. The location of the YSH borehole is remarked as the yellow star used for monitoring the strain variation continuously by minutes and hours. There are 38 earthquakes indicated by the white dots with magnitudes ranging from M 3.0 to M 7.3 that occurred between January 1, 2009 and December 31, 2018 (Table 1). (b) Zoomed map of the study area. The green bars indicate the azimuth of the S_H inverted by the focal mechanism of $M_s \geq 4.8$ earthquakes (except for EQ3) during the abovementioned period. The bar lengths are proportional to the earthquake magnitudes.

Table 1 Earthquakes ($M \geq 3$) occurring between 1 January 2009 and 31 December 2018 near the Ganzi-Yushu fault (The data are provided by the China Earthquake Data Center) and the azimuth of S_H, computed based on focal mechanism data from the CMT catalog (Ekström et al. 2012).

No.	Time	Long.	Lat.	Depth	Magnitude	Azimuth of S_H/(°)

		/ °E	/ °N	/km		
EQ1	14/04/2010 05:39:58	96.59	33.11	15	M_S 4.8	74
EQ2	14/04/2010 07:49:36	96.59	33.22	14	M_S 7.3	78
EQ3	14/04/2010 08:01:15	96.89	33.00	6	M_S 4.9	
EQ4	14/04/2010 09:25:16	96.57	33.22	17	M_S 6.4	67
EQ5	14/04/2010 20:19:30	96.99	32.97	10	M_L 3.7	
EQ6	15/04/2010 12:00:06	96.99	33.01	10	M_L 3.6	
EQ7	16/04/2010 02:30:17	96.76	33.09	10	M_L 3.7	
EQ8	16/04/2010 06:37:07	96.98	32.99	10	M_L 3.2	
EQ9	17/04/2010 07:04:12	96.49	33.17	7	M_S 3.6	
EQ10	21/04/2010 04:23:38	96.74	33.08	10	M_L 3.2	
EQ11	29/04/2010 00:48:36	96.52	33.19	10	M_L 4.6	48
EQ12	29/04/2010 00:53:52	96.52	33.21	4	M_L 3.4	
EQ13	29/05/2010 10:29:49	96.21	33.26	10	M_S 5.9	30
EQ14	29/05/2010 09:36:00	96.24	33.28	7	M_L 3.2	
EQ15	29/05/2010 10:43:53	96.22	33.31	9	M_L 3.8	
EQ16	29/05/2010 10:45:26	96.22	33.31	10	M_L 3.3	
EQ17	29/05/2010 10:46:53	96.20	33.32	5	M_L 3.4	
EQ18	29/05/2010 11:11:16	96.18	33.30	10	M_S 4.0	
EQ19	01/06/2010 09:41:03	96.18	33.29	9	M_S 3.2	
EQ20	02/06/2010 10:36:24	96.23	33.27	10	M_L 3.3	
EQ21	03/06/2010 13:06:19	96.20	33.34	8	M_L 3.3	
EQ22	03/06/2010 13:35:42	96.22	33.31	11	M_S 5.4	43
EQ23	03/06/2010 13:46:57	96.31	33.28	10	M_S 4.3	
EQ24	04/06/2010 04:47:04	96.20	33.31	7	M_S 5.0	36
EQ25	04/06/2010 10:00:45	96.11	33.30	4	M_S 3.7	

EQ26	07/06/2010 00:42:42	96.20	33.31	10	M_s 4.8	36
EQ27	07/06/2010 01:28:29	96.24	33.32	6	M_s 3.7	
EQ28	07/06/2010 01:28:29	96.20	33.29	10	M_s 4.0	
EQ29	10/06/2010 02:31:27	96.18	33.33	9	M_s 3.3	
EQ30	15/06/2010 16:08:30	96.31	33.38	6	M_s 4.4	
EQ31	18/06/2010 22:10:16	96.20	33.32	10	M_s 3.4	
EQ32	08/09/2010 04:50:59	96.28	33.28	30	M_s 4.8	43
EQ33	08/09/2010 09:58:08	96.26	33.30	10	M_L 3.7	
EQ34	04/10/2010 15:58:28	96.20	33.31	10	M_L 3.0	
EQ35	27/11/2010 07:07:02	96.03	33.35	10	M_L 3.2	
EQ36	07/08/2014 18:28:39	96.60	33.18	7	M_s 3.7	
EQ37	13/06/2015 13:14:28	96.56	33.23	10	M_s 3.5	
EQ38	01/11/2017 13:33:38	96.18	33.35	9	M_s 4.0	

3 Observation method and data

YRY-4-type four-gauge borehole strainmeters (FGBS) manufactured by Chi et al. (2009) have been largely deployed by China Earthquake Administration to monitor the temporal changes in horizontal strain in response to the U.S. Plate Boundary Observatory project. There are approximately 40 YRY-4-type FGBS stations in China where data can be monitored with sampling rates of one per minute or one data point per hour (Qiu et al. 2013). The data obtained from these borehole strainmeters have been used in many scientific studies (Qiu and Shi 2004; Qiu et al. 2007, 2011). We selected one of these stations, namely the YSH borehole, which was located close to the Yushu earthquake epicenter and approximately 80 meters north from the Ganzi-Yushu fault (Fig. 1) to analyse strain data in parallel with aftershock sequences. In this way, strain variation in relation to the earthquake preparation process can be investigated (Qiu et al. 2011). Since the YSH borehole strainmeter has been in operation since January 3, 2008, strain (ε) variation associated with the Yushu earthquake which occurred on April 14, 2010 can be investigated (Fig. 2b). The YSH borehole strainmeter was installed at a depth of 39.5 m with four-component gauges that are horizontally emplaced with 45-degree angles, to measure strain changes in borehole diameter with sampling rates of one data point per minute and one per hour (Fig. 2a). The depth was selected due to the theoretical model used to derive strain values assuming that the vertical normal stress is zero (Qiu et al. 2013). Based on the measured strain data, the principal strain orientation (φ) was derived as (Qiu et al. 2013)

$$\varphi = \frac{1}{2}\arctan\left(\frac{\varepsilon_2 - \varepsilon_4}{\varepsilon_1 - \varepsilon_3}\right) + \theta_1 \qquad (1)$$

where ε_i (i = 1, 2, 3, 4) are the measurements by the four gauges installed in the borehole and θ_1 is the azimuth of ε_1 gauge. We assumed that the orientation of S_H corresponds to φ, taking into consideration that the elastic modulus of the rock mass remains constant, as the YSH borehole strainmeter was installed in intact granite rock.

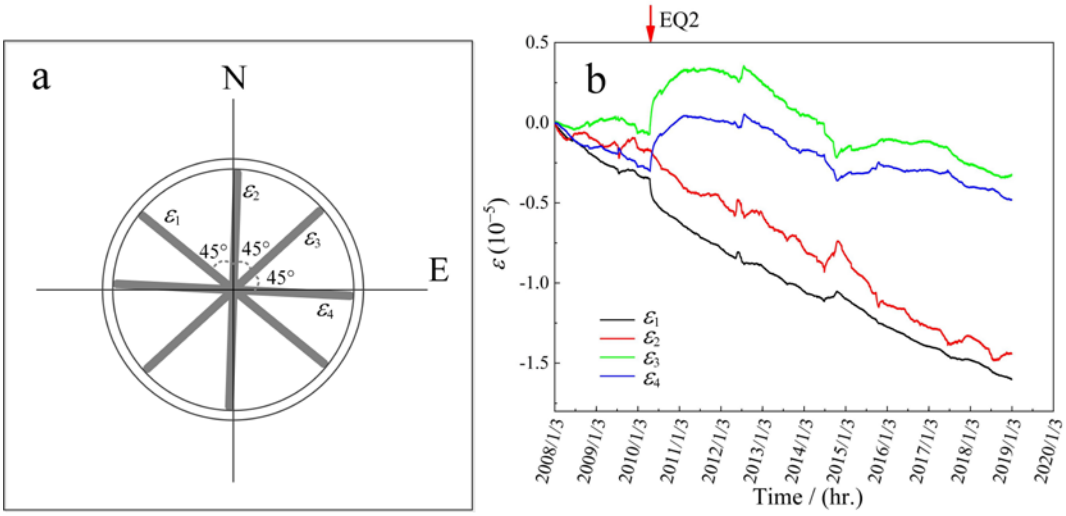

Fig. 2 (a) Alignment of the gauges (grey bars) for strain measurement in the YSH borehole; (b) Temporal (hourly-based) changes in the strain (ε) from January 3, 2008 to December 31, 2018 in YSH borehole. The red arrow on the top indicates the time of the Yushu mainshock (*M*s 7.3 see Table 1).

To analyze the relationship between the reorientation of S_H and the occurrence of the earthquake involving the Ganzi-Yushu strike-slip fault, we present the change of the orientation $\Delta\theta$ of S_H and the cumulative magnitude (*M*s) of earthquakes from January 3, 2008 to December 31, 2018 (Fig. 3). We convert local magnitude M_L in Table 1 to surface-wave magnitude M_S using the empirical relationship given as (Gutenberg and Richter 1956)

$$M_s = 1.27\left(M_L - 1\right) - 0.016 M_L^2 \qquad (2)$$

The value of $\Delta\theta$ increases substantially from approximately -33 degrees to -11 degrees, more than 20 degrees, while the cumulative Ms increases by about 134 N·m from April 14, 2010 to November 27, 2010 (Fig. 3a). This implies that the S_H axis observed in the YSH borehole rotated 22 degrees clockwise. If we zoom into the variation of data sampled per minute on the day the Yushu earthquake (EQ2) occurred, $\Delta\theta$ first decreases by about 1 degree and then increases by 6 degrees, while the cumulative Ms increases by 23 N·m in the same time period (Fig. 3b). Although the co-seismic data were not recorded because of broken power supply by earthquake interruption (Fig. 3b, gap in data), the final $\Delta\theta$ was about 5 degrees from the original state.

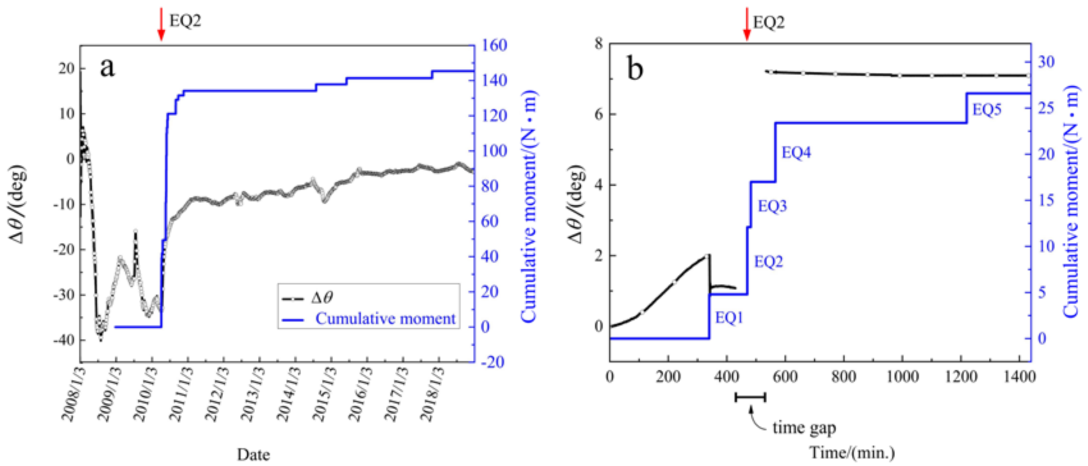

Fig. 3 The $\Delta\theta$ and the cumulative magnitude of earthquakes occurring near the Ganzi-Yushu fault vs. monitoring date from 3 January 2008 to 31 December 2018 with a sampling rate of per hour (a). The zoomed time window sampling rate of per minute on the day of the Yushu mainshock occurring on 14 April 2010 (b). The black bar below shows the gap (103 minutes) in data due to the broken power supply by earthquake interruption. The red arrow on the top indicates the time of the Yushu mainshock.

4 Numerical model and methodology

4.1 Particle Flow Code 2D

For numerical modelling of stress evolution around a seismogenic fault associated with its dynamic rupture, we used Particle Flow Code 2D v4 (PFC2D v4) which is a commercial software of Itasca Consulting Group (Itasca 2008) developed on the basis of Discrete/Distinct Element Method, DEM (Cundall 1971; Cundall and Strack 1979). The concept of DEM is implemented in PFC and the way in which PFC is applied for simulation of rock mechanics problems is referred to as Bonded Particle Modelling (BPM, Potyondy and Cundall 2004). PFC has been, since its release in late 1990s, applied to rock mechanics and rock engineering problems due to its strong advantage that modelling of a system with large populations of particles require only modest amounts of computer memory and physical instability (large deformation problems, e.g. landslide, rock blasting, rock fall) can be modelled without numerical difficulty. Further details on BPM application in rock mechanics problems can be found in Potyondy and Cundall (2004).

Lately, the BPM method has evolved significantly by implementation of hydro-mechanical (HM) and thermo-mechanical (TM) coupling concepts. For HM coupling, PFC has been applied widely for simulation of fluid injection induced seismicity in the fields of deep geothermal energy (Hazzard et al. 2002; Hofmann et al. 2016a; Yoon et al. 2014b, 2015a), shale gas hydraulic fracturing (Al-Busaidi et al. 2005; Hofmann et al. 2016b), and waste water disposal (Yoon et al. 2015b). For TM coupling, PFC has been applied to geological disposal of spent nuclear fuel and radioactive wastes (Yoon et al. 2016; Yoon and Zang 2019).

4.2 Modelling of fault dynamic rupture

Using PFC2D, we generated a geological model representing the Ganzi-Yushu site as shown in Fig. 1. The model size is 220 ×180 km^2 (Fig. 4a), and the areal space is packed with 388,987 disks with diameters ranging between 130 m to 215 m (Fig. 4b). To investigate the temporal and spatial variation patterns of S_{H} along the study fault, we set measurement circles in the moving direction (Fig. 4b, stress circles (2) and (5)), opposite moving direction (Fig. 4b, stress circles (3) and (4)), and tip of the fault (Fig. 4b, stress circles (1) and (6)); we set 6 measurement circles symmetrically lay on the perpendicular profile line in the middle of the fault (Fig. 4b, stress circles (7) to (12)) and one measurement circle at the YSH borehole position (Fig. 4b, stress circles (13)). To systematically investigate the effect of the fault geometry (e.g., linear fault and curved fault) and the effect of off-fault host rock damage on the stress reorientation, we setup four scenarios of fault dynamic rupture: 1) linear fault with elastic rock mass (LE); 2) linear fault with elasto-plastic rock mass (LEP); 3) curved fault with elastic rock mass (CE) and 4) curved fault with elasto-plastic rock mass (CEP). We used enhanced parallel bond model (Yoon et al., 2014b) and smooth joint contact model (Ivars et al. 2011) for the host rock and the (segmented) fault system, respectively. The failure of the parallel bond and the smooth joint contact is governed by the Mohr-Coulomb failure criterion of which the parameters are listed in Table 2.

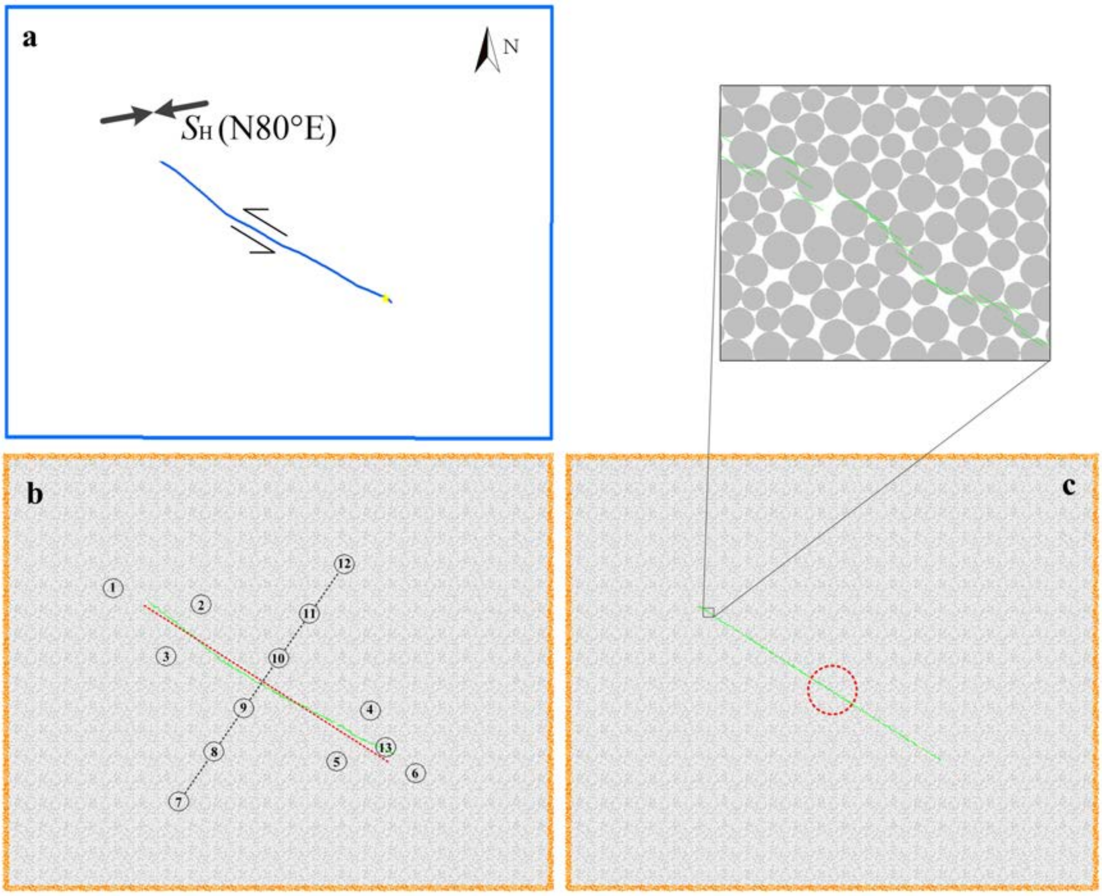

Fig. 4 a) Geometry of the investigated Ganzi-Yushu fault. The yellow star marks the location of the observation borehole. b) Particle curved fault model with monitoring stress circles (radius = 4000 m). Circle (13) is located exactly at the borehole position. The circles (7) to (12) lay on the perpendicular profile line (black dotted line). The red dotted line indicates the linear fault geometry applied in the numerical modelling. c) Particle linear fault model with measurement circle indicated by red dotted circle for converging to target stress values. The green curve and green line represent the curved fault (b) and linear fault (c), respectively.

To mimic a fault dynamic rupture, we used the modelling approach as described in Yoon et al. (2017). The approach for simulating a dynamic fault rupture first starts with locking the fault by strengthening the smooth joint bond strength (tensile and cohesion). Second, the model is compressed by servo-controlling the velocities of the boundary layer particles (orange colored in Fig. 4b). The servo-control process continues until stress components (σ_{xx}, τ_{xy}, σ_{yy}) that are monitored in the stress measurement circle (Fig. 4c) located at the model center reach the target stress magnitudes and orientations. We assumed that the 2D model section is located at depth of 2000 m, and therefore, the stresses in situ are 64 MPa and 38 MPa for the maximum and minimum horizontal stress S_H and S_h, respectively. The stress magnitudes (in MPa) are calculated by the following equations based on the in-situ stress measurements in Qinghai Tibet block, China (Yang 2013),

$$S_{\mathrm{H}} = 0.0292Z + 5.185 \tag{3}$$

$$S_{\mathrm{h}} = 0.0172Z + 3.681 \tag{4}$$

where, Z is the depth (m).

The stress orientation applied here is mainly based on the Global Positioning System (GPS) velocity field near the study region, and the average direction of the GPS velocity determined by seven stations within the study region shows an angle anticlockwise about 10° to the horizontal axis (E-W), which indicates that the orientation of in-situ S_H is nearly N80°E (Zheng et al. 2017). To simulate the 10° deviation of the in-situ S_H orientation from the horizontal axis, the velocities of the boundary layer particles (Fig. 4b, orange colored) are servo-controlled so that shear stress develops within the stress measurement circle at the model center (Fig. 4c). The resulting principal stresses therefore deviates 10° from the model axes. The magnitudes of the in-situ stress components, i.e., normal stresses (σ_{xx} and σ_{yy}) and shear stress (τ_{xy}) to be used for servo-controlling the velocities of the boundary layer particles, in the stress measurement circle at the model center are determined by Mohr circle stress analysis (for details, we refer to Yoon et al., 2014a).

In a third step, dynamic faulting was simulated by unlocking the fault. The strained fault was unlocked by instantaneous reduction of the particle bond strength mimicking dynamic fault rupture and energy release. Upon fault unlock, a seismic wave generates, propagates, and attenuates due to damping. The local damping coefficient of 0.7 is applied to particles to mimic attenuation of seismic energy that propagates in a form of a seismic wave generated at the seismic source (rupturing fault). In future study, spatial variation of the damping coefficient will be considered by taking into account the site-specific geological heterogeneity conditions. This approach of simulating fault dynamic rupture by unlocking the fault strength and stiffness is similar to the modelling approach by Bilham and King (1989), Saucier et al. (1992) and Fälth et al. (2015). Additionally, the friction coefficient, friction angle and dilation angle of the smooth joints, listed in Table 2, are lowered to 10% of their initial values, taking into account the fault asperity loss by dynamic rupture (Yoon et al., 2017).

Table 2 Modelling properties of the rock mass and the Ganzi-Yushu fault.

Parameters	Value	References
Rock mass by parallel bond model	—	—
Density	2720 kg/m^3	Yang (2013)
Poisson's ratio	0.25	Yuan (2017)
Elastic modulus	70 GPa	Yuan (2017)
Friction angle	50 °	
Cohesion	30 MPa	
Tensile strength	10 MPa	
Fault by smooth joint model	—	—
Normal stiffness	600 GPa/m	
Shear sfiffness	50 GPa/m	
Friction coefficient	0.2	
Tensile strength	0.2 MPa	
Cohesion	1 MPa	
Friction angle	30 °	
Dilation angle	3 °	

5 Results

Fig. 5 shows the fault slip displacement shortly (90 seconds) after rupture initiation for each scenario. Slip displacements of LEP and CEP scenarios are lower compared to the corresponding elastic host rock scenarios (LE, CE). The difference is due to the off-fault damage, where the co-seismically-generated dynamic energy is consumed, resulting in less slip along the fault trace as compared with the elastic host rock scenario. The linear fault model shows a parabolic profile of co-seismic slip displacement versus fault length, whereas the curved fault model shows an asymmetric slip distribution, which reasonably well follows the slip profiles observed along natural earthquake faults (Manighetti et al. 2005, 2007, 2009).

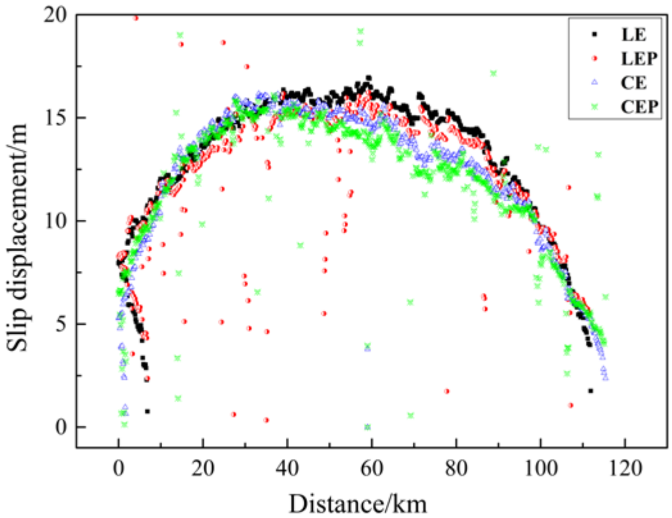

Fig. 5 Co-seismic slip distribution of the fault trace embedded in the elastic and elasto-plastic host rock masses at 90 seconds after rupture initiation. The coordinate origin is the left tip of the fault trace.

The evolution of the stress quadrants is illustrated in Fig. 6. When the northeastern block of the fault slips NE, the stress in the moving direction will increase, resulting in a compressive stress increase (compression quadrant). The force in the opposite direction will drop, resulting in a tensile stress increase (dilatation quadrant). The evolution of the compression and dilatation quadrants with respect to the other three scenarios (LEP, CE and CEP) is similar as shown in the supplementary material, see Online Resource 1.

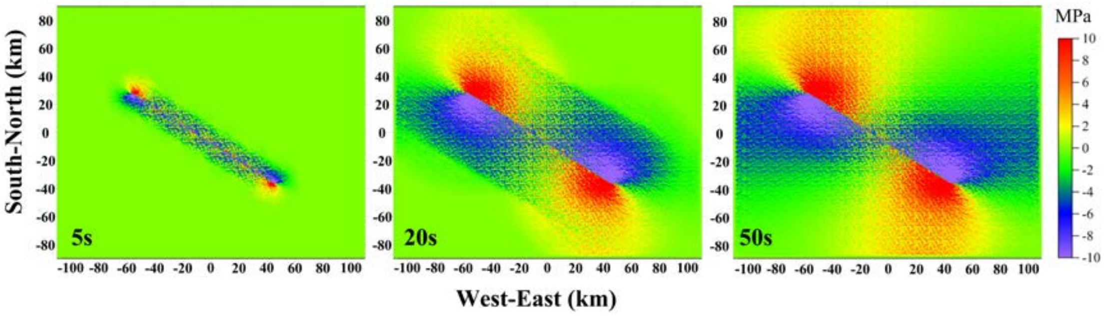

Fig. 6 Spatiotemporal evolution of compression (red) and dilatation (blue) stress quadrants for the LI scenario.

As can be clearly seen from Fig. 7, the $\Delta\theta$ variation for the four scenarios typically show different patterns. However, no obvious changes in $\Delta\theta$ could be observed in response to the strain energy release after approximately 50 s. The $\Delta\theta$ measured in the compression quadrants for each scenario drops substantially from approximately 0° to -10°, exhibiting approximately 10° counterclockwise rotation (Fig. 7, stress circles (2) and (5)). The azimuth change over time for elasto-plastic rock mass shows some undulations, mainly due to off-fault damage (Xu and Arson 2015), seen in Fig. 8b. The undulations in the initial part of the curve may be due to dynamic effect, where the stress at the location is affected by the dynamic wave passing by (Belardinelli et al. 1999). However, the asymptotic values at t > 50 s are similar to the corresponding values of faults with elastic rock mass. The curved faults show larger $\Delta\theta$values than the linear faults. This indicates that the curvature of the fault has a more significant impact on S_H rotation than the host rock properties.

The $\Delta\theta$ values measured in the dilatation quadrants for each scenario show first a sharp decrease with subsequent increases to a stable value corresponding to the starting value (Fig. 7, stress circles (3) and (4)). This indicates that the stress azimuth rotates back to the original state after the earthquake occurred in the dilatation quadrants. The LE scenario shows the largest negative variation value, reaching more than -8° while the CE scenario shows the largest positive variation value (Fig. 7, stress circles (3) and (4)). Though the azimuth for each scenario increases to a stable value, only the scenarios regarding curved faults, i.e., CE and CEP result in a positive value. This implies that only the azimuth of S_H for the CE and CEP scenarios increase after the earthquake compared to the other scenarios (Fig. 7, stress circles (3) and (4)). The asymptotic values of stress azimuth at times larger than

50 s for elasto-platic rock mass are less by about one degree than the asymptotic values for stress azimuth for elastic rock mass. This may be due to lower tensional force caused by the off-fault damage in CEP scenario (Fig. 8b) as compared to the CE scenario (Fig. 8a).

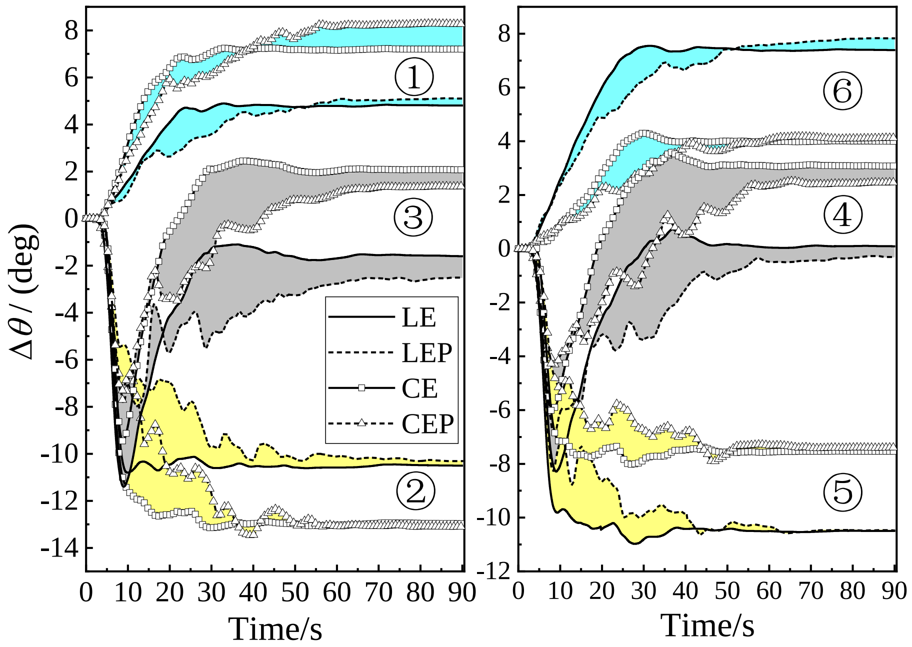

Fig. 7 Temporal changes of $\Delta\theta$ for each scenario. The stress variation observed at the tip of the fault (stress circles (1) and (6)) indicated by cyan region. The stress variation observed in the compression quadrants (stress circles (2) and (5)) indicated by yellow region. The stress variation observed in the dilatation quadrants (stress circles (3) and (4)) indicated by grey region.

The $\Delta\theta$ values measured at the tip of the fault for the four scenarios increases substantially and subsequent approaches a nearly constant plateau value. However, the maximum $\Delta\theta$ value for the curved faults (CE and CEP) measured at the northwest tip of the fault is approximately two times larger than that at the southeast tip of the fault (Fig. 7, stress circles (1) and (6), refer to Fig. 4b for the measurement circle locations), which is probably due to the curved geometry of the fault. As can be clearly seen from Fig. 4b, due to the bending effect of the curved fault, the measurement circle (1) located at the northwest tip of the fault is mostly within the dilatation quadrants, while the measurement circle (6) located at the southeast tip of the fault is mostly within the compression quadrants. As illustrated above, the maximum $\Delta\theta$ value finally increases within dilatation quadrants as compared to the decrease within compression quadrants. The stress change is therefore asymmetric, i.e. it is larger at one end of the curved fault as compared with the other end.

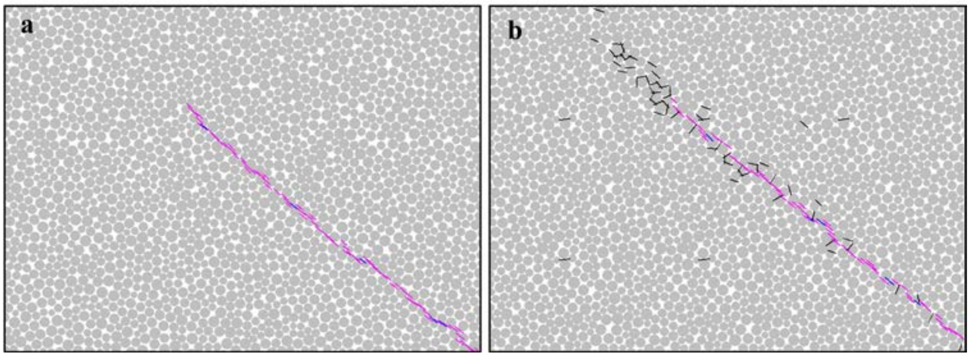

Fig. 8 Close-up view of cracking (smooth joints in magenta and blue) after earthquake in CE scenario (a) and in CEP scenario (b). The black bar indicates the off-fault damage.

Fig. 9 shows the developments of $\Delta\theta$ for four scenarios measured in the measurement circle (13). First, the orientation values drop significantly, and then increase to a stable value, which are consistent with those measured in the dilatation quadrants (Fig. 7, measurement circles (3) and (4)). Note that the maximum positive magnitudes of $\Delta\theta$ for each scenario measured in the measurement circle (13) are larger than that measured in the measurement circle (4) presumably due to the position near to the fault, i.e., the approximate distance is 80 m from the YSH borehole to the fault. In comparison to the field observation presented in Fig.3b, the magnitude of $\Delta\theta$ first decreases by about 6 degrees and then increases by 10 degrees for the CEP scenario within 50 s. It seems that the initial drop in model is much larger than that in borehole observations. The reason for this difference is possibly due to the fact that we assume the fault rupture hypocenter is at the depth of the stress measurement circle (2D plane), whereas the Yushu earthquake hypocenter is at larger depth and the strain measurement was done at shallow depth. Therefore, the distance between the EQ hypocenter and the gauge measurement is relatively large in nature and relatively small in the model, which may explain the larger initial stress drop in the model. In addition, the field data were recorded with sampling rates of one per minute (Fig.3b), and unfortunately, we cannot resolve co-seismic strain data during the occurrence of EQ2. If we cumulatively add the energy of four events (EQ1, EQ2, EQ3 and EQ4) in one time step of strain energy release, the $\Delta\theta$ variation modeled during the activation process of the smooth joints agrees with in-situ observations in the YSH borehole.

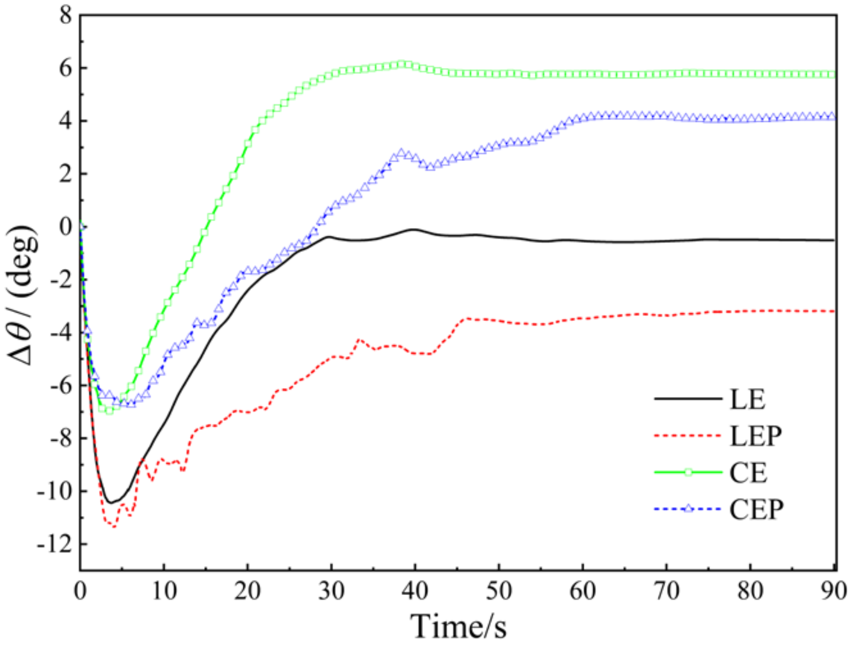

Fig. 9 Temporal changes of $\Delta\theta$ for each model scenario at the location of the YSH measuring borehole (stress circle (13)).

In Fig. 10, we shift the focus to the maximum values of $\Delta\theta$ as a function of distance perpendicular to the fault. The maximum $\Delta\theta$ variation trend for all four scenarios is almost similar; that is, the largest $\Delta\theta$ value occurs near the fault, and it drops as the distance increases from the fault. The maximum $\Delta\theta$ variations for linear faults (e.g., LE and LEP), which are not symmetric to the fault, are likely attributed to the location of the fault in the model. We conclude that the further the measurement distance is from the fault, the smaller the magnitudes of maximum $\Delta\theta$ are, i.e., at 50 m distance from fault core, the mean maximum $\Delta\theta$ drops by 81%, 86%, 79% and 85% with distance from the fault for scenarios LE, LEP, CE and CEP, respectively (Fig. 10).

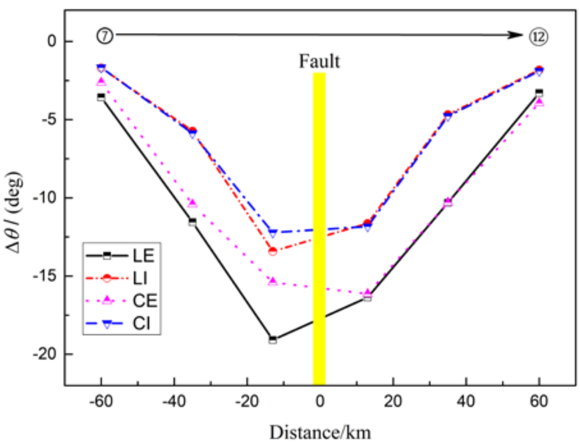

Fig. 10 Maximum $\Delta\theta$ vs. distance from the fault on the perpendicular profile line (stress circles (7) to (12)).

6 Discussion

We mainly focused on numerical modelling of reproducing such spatio-temporal changes in the orientation of local maximum horizontal stress at several locations along the trace of a rupturing fault. The effects of fault geometry and off-fault damage were investigated with discrete element numerical simulations using a single and segmented fault surrounded by elastic and elasto-plastic host rock. By comparing a unique (although not continuous) field data set recorded by a borehole strain meter close to a pure strike-slip fault, we developed a synoptic geomechanical model for the stress redistribution in such a situation. We found that the $\Delta\theta$ values observed in the YSH borehole near the Ganzi-Yushu fault first decreases and then increases substantially with increasing cumulative magnitude of earthquakes occurring near the Ganzi-Yushu fault. The dilatation and compression stress quadrants can be gradually formed along the strike-slip fault after activation, which is consistent with the strike-slip fault dislocation source solution obtained by Okada (1992). However, the Okada model closed form solution is limited to elastic rock material and a straight fault geometry. In our approach, dynamic and inhomogeneous variations of stress pattern along a segmented strike-slip fault with off-fault damage is quantified. As a result of the relative plate slip motion, the $\Delta\theta$ observed in the compression quadrants, dilatation quadrants, and at the tips of this strike-slip fault show different temporal variation and reach a different asymptotic value. The fault releases energy that can temporally generate a compressive stress field within the compression quadrants and form a local field stress through the resultant stress with the tectonic stress field. However, a tensional stress field is generated within the dilatation quadrants and form another different local stress field. Compared with previous studies, we used an innovative segmented fault approach for a straight and curved fault geometry using smooth joints. This allows to account for off-fault damage which is frequently observed along natural faults, e.g. in terms of exponential decrease of microcrack damage with distance from fault core (Vermilye and Scholz, 1998; 1999). The maximum magnitudes of the $\Delta\theta$ values drop with distance from the fault. It is important to note that the temporal variations of S_{H} associated with earthquakes observed by the FGBS in the YSH borehole are compatible with the numerical modelling results measured in the dilatation quadrants.

Hardebeck and Hauksson (2001) pointed out that the 1992 Joshua Tree and Landers earthquakes induced substantial rotations of S_H along the SAF. Different temporal variation patterns are observed in the different regions, i.e., increasing for the Emerson and Homestead Valley and decreasing for the Johnson Valley to a relatively stable value (Hardebeck and Hauksson 2001). The increase in the azimuth of S_H in the Emerson region is consistent with our modelling results within the dilatation quadrants. However, we may not exactly differentiate the temporal evolution of the S_H orientation in the compression and the dilatation region associated with the SAF from this case since the bins used for focal mechanism inversion straddle the fault trace irrespective of the quadrants generated along the strike-slip fault (Hardebeck and Okada 2018). The $\Delta\theta$ values observed in dilatation quadrants drops at first, then increases sharply and eventually reaches a stable value, which indicates that the azimuth of the S_H will have a counterclockwise rotation which will later reverse itself. This is in agreement with the stress variation pattern observed in the central zone of the Eastern California Shear Zone (ECSZ) (Hauksson 1994).

Yin and Rogers (1995) obtained a general rotation angle ($\Delta\alpha$) solution for strike-slip faulting. For positive $\Delta\alpha$, the maximum stress axis rotates toward the normal to the fault, while for negative $\Delta\alpha$, the axis rotates away from the normal to the fault. Based on the magnitudes of 38, 54, and 64 MPa for the minimum, intermediate and maximum principal stresses respectively applied in our model, the stress ratio (δ) is equivalent to ～0.62. Since the angle between the Ganzi-Yushu fault and the far-field S_H axis is approximately 42°, the average stress drop ratio is approximately 0.95 and 0.90 for linear faults and curved faults, respectively. This implies that the azimuth variation of the S_H increases during the release of the strain energy. When applying this solution to our case, one limitation should be noted: the areas close to and beyond the edge of the rupture area are not applicable (Yin and Rogers 1995). However, we can obtain some understanding of the stress rotation with respect to the YSH borehole observation, where the azimuth variation increases to a relatively stable value. It should be pointed out that Yin and Rogers' solution cannot reflect the first drop pattern in the evolution of the stress azimuth variation in the modelling results and in-situ observation data. It is more probable that the stress drop involving the Yushu earthquake reduced the shear stress acting on the fault, causing stresses to rotate counter-clockwise (Bohnhoff et al. 2006). Additionally, the stress rotations observed in the compression quadrants in our model drop dramatically to a relatively stable value, which are inconsistent with the rotation angle predicted by Yin and Rogers (1995). This discrepancy probably arises from the stress concentration gradually formed in the compression quadrants (Fig. 6).

One explanation for this discrepancy is given in the synoptic Fig. 11. During co-seismic slip, the fault releases energy that can temporally generate a compressive stress field (grey shaded area) within the compression quadrants and form a local field stress, S_H (post-Eq) through the resultant stress with the tectonic stress field, S_H (pre-Eq). Thus, the resultant stress orientation shows a counterclockwise rotation angle ($\Delta\theta$) away from the far-field tectonic stress, S_H (pre-Eq). However, a tensional stress field (orange shaded area) is generated within the dilatation quadrants and form a local stress field, S_H (post-Eq), indicating a clockwise rotation angle away from the S_H orientation prior to the earthquake occurrence (pre-Eq). It should be noted that there is an initial drop of $\Delta\theta$ within the dilatation quadrants. This can be explained with the local stress barriers or blocks formed ahead of the dilatation stress quadrants resulting from the compressive stress (red dotted arrows), but these will gradually will be tapered as fault slip motion continues.

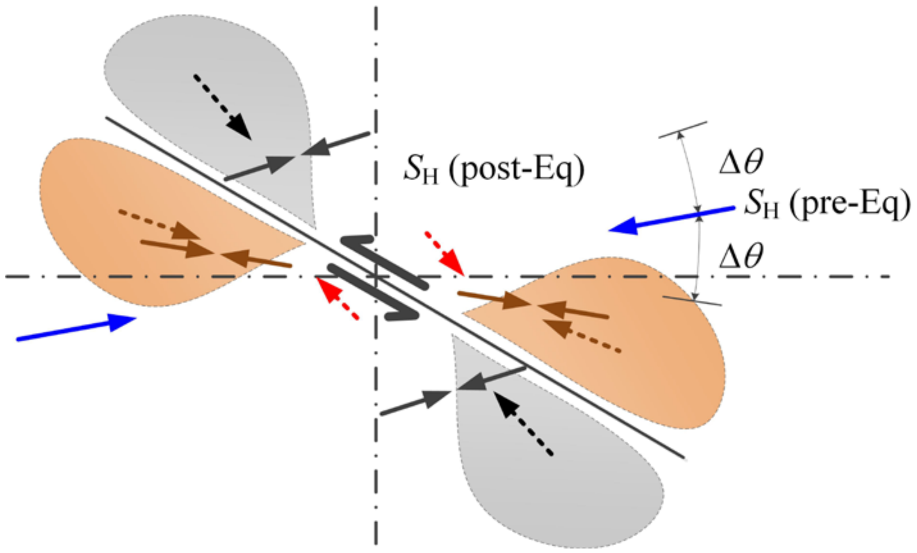

Fig. 11 Synoptic picture of the assumed stress reorientation relative to the slip motion of the left-lateral strike-slip fault. Black solid arrows indicate the orientation of the maximum horizontal principal stress within compression quadrants after earthquake. Orange solid arrows show the orientation of the maximum horizontal principal stress within dilatation quadrants after earthquake.

The spatial distribution of maximum $\Delta\theta$ value substantially differs along the profile perpendicular to the fault, i.e., the maximum $\Delta\theta$ drops with the distance from the fault. The discrepancy in the stress rotations between near- and far-field agrees with the in-situ stress measurements along the SAF, where the orientation of the S_H measured in the far-field is NNE. However, the azimuth of the S_H measured in the near field approximately rotates to EW north of the fault and NW south of the fault (Sbar et al. 1979), perpendicular to the strike of the SAF in its immediate vicinity (Fuchs and Muller 2001; Zoback et al. 1987). Stress reorientation patterns near the ground surface can be precisely and continuously recorded using FGBS within YSH borehole arising from relative plate motion with respect to the Ganzi-Yushu fault. The co-seismic stress reorientation data observed only from one borehole with respect to the Ganzi-Yushu fault are a weak boundary condition. We suggest that more FGBS be used to observe the reorientation of S_H near the crustal surface with high resolution within the compression and dilatation quadrants along the strike-slip faults. Also, one can think about measuring strain and stress in deep boreholes close to the fault if any boreholes become available in the future. Co-seismic slip distribution shows more drastic change when the fault is curved (curved fault) and off-fault damage is simulated (elasto-plastic rock mass). Natural faults are never continuous, but rather show complex structures along its trace, such as pull-apart regions, rotated blocks, isolated lenses, etc. as shown in literature by Choi et al. (2012). Representing such structural complexity of natural faults by smooth joint contact model in a bonded particle assembly is a first order approach to complex fault zone architecture. Also, Aochi and Madariaga (2003) demonstrated that slip profile of the Izmit Turkey earthquake in 1999 was better modelled and match with better with observations, when the fault is represented as curved and segmented, compared to linear and continuous. In this 2D modelling, we assumed that the stress changes near the Ganzi-Yushu fault is mainly associated with Yushu main earthquake (EQ2). The existing additional faults may have moved by the Yushu earthquake and may have influenced the stress reorientation at YSH borehole. However, as seen in the earthquake hypocenter map, those fault traces beside the Ganzi-Yushu fault do not host any of the earthquake $M > 3$ hypocenters. Therefore, we limit our modelling to only the trace of Ganzi-Yushu fault representing major seismo-tectonic energy release in the study area. Simulating multiple fault traces and investigating the effect of the additional faults on the co-seismic stress distribution and stress orientation at YSH borehole are suggested for future study. In addition, this 2D model for co-seismic slip provides a first-order estimate of the impacts on the local stress field of such strike-slip motion, assuming a full fault trace rupture. An earthquake fault seldom ruptures in its entire plane. Partial and segmented ruptures will be taken into account in future modelling. Accordingly, the modelling of stress orientation associated with the YSH borehole is a qualitative analysis rather than a quantitative estimation. The present study suggests that a PFC 3D model taking into account the detailed complex geological conditions and the multistage rupture process related to the Ganzi-Yushu fault is needed. We do not consider the effect of fluids. The presence of fluid in the rock mass and in the fault could have different effects on the overall behavior of stress reorientation around and near to a rupturing fault. If the fault is fluid filled, the fault slips earlier and slowly during the tectonic loading compared to the fluid-free fault situation. In addition, the fluid-filled fault dilation results in normal stress increase. Normal stress increase would compact the pore volume, and due to fluid incompressibility and trapped pore fluid, the rock mass can become over-pressurized. Over-pressurized, trapped fluid in a fault can result in (a) fault tip propagation, (b) local stress concentration and (c) in stress reorientation around the fault (before the dynamic rupture) due to stress shadowing effect (Yoon et al. 2015a). If the fault is partially fluid-filled or filled heterogeneously with fluid, the effect of fluid presence would be more complex.

7 Conclusion

The $\Delta\theta$ values observed with the FGBS system in the YSH borehole near the Ganzi-Yushu fault first decreased and then increased substantially to an asymptotic value in response to the Yushu earthquakes. In order to interpret this stress reorientation phenomenon and provide insights into the spatiotemporal reorientation pattern of S_{H} regarding the strike-slip fault during earthquake occurrence, we present a discrete element modelling using PFC2D and set up four scenarios of fault dynamic rupture (LE, LEP, CE and CEP). The modelling of $\Delta\theta$ variation patterns during the activation of the smooth joints for each scenario agrees with in-situ observations in the YSH borehole during earthquake occurrence, which indicates that the stress rotation contributed to the Yushu earthquake. The modelling reveals that dilatation and compression quadrants are formed around a strike-slipping fault, resulting in different spatiotemporal changes of the $\Delta\theta$ value. The $\Delta\theta$ value in the compression quadrants drops substantially by co-seismic slip then finally approaches an asymptotic value. In the dilatation quadrants, $\Delta\theta$ value drops by co-seismic slip, then increases sharply and finally reaches a stable value. During co-seismic slip, the fault releases energy that can temporally generate a compressive stress field within the compression quadrants and form a local field stress through the resultant stress with the tectonic stress field. However, a tensional stress field is generated within the dilatation quadrants and form a local stress field indicating a clockwise rotation angle away from the S_H orientation prior to the earthquake occurrence. In addition，the $\Delta\theta$ value decreases with increasing distance from the location of rupture source. The structural complexity and off-fault damage by co-seismic fault slip have a significant impact on the stress field alteration near the rupturing source. In order to understand the stress reorientation in more detail within the quadrants, we suggest that higher resolution FGBS data should be used in combination with deformation measurement methods (e.g., InSAR measurements), which can help to understand the stress reorientations before, during and after occurrence of large earthquakes.

Acknowledgements

We would like to thank Prof. Ove Stephansson for his thoughtful advice and constructive guide. We thank Prof. Günter Zimmermann, Dr. Hannes Hofmann and Marton Pal Farkas for their helpful discussions. We also thank Dr. Alireza Hassanzadegan and Dr. Djamil Al-Halbouni for their constructive feedback. We appreciate Dr. Anne Strader who proofread the manuscript. This work has been supported by National Natural Science Foundation of China (Grant No. 41807270), Key Program for International S&T Cooperation Projects of China (Grant No. 2016YFE0205100) and Earthquake Spark Program Project (Grant No. XH19070). This work was performed during the first author’s visit to the Helmholtz Centre Potsdam GFZ German Research Centre for Geosciences, supported by the China Scholarship Council. We thank Geospatial Data Cloud for making GDEMDEM data freely available on their website. We are grateful to two anonymous reviewers and the associate editor for their constructive comments and suggestions that greatly improved the paper.

Reference

Al-Busaidi A, Hazzard JF, Young RP (2005) Distinct element modeling of hydraulically fractured Lac du Bonnet granite. J Geophys Res 110: B06302. https://doi.org/10.1029/2004JB003297

Agnès H, Kagan YY, Jackson DD (2005) Importance of small earthquakes for stress transfers and earthquake triggering. J Geophys Res 110(B5).

Aochi, H (2003) The 1999 Izmit, Turkey, Earthquake: Nonplanar Fault Structure, Dynamic Rupture Process, and Strong Ground Motion. B Seismol Soc Am 93(3):1249-1266.

Barton CA, Zoback MD (1994) Stress perturbations associated with active faults penetrated by boreholes: possible evidence for near - complete stress drop and a new technique for stress magnitude measurement. J Geophys Res 99(B5):9373-9390. https://doi.org/10.1029/93JB03359

Bilham R, King G (1989) The morphology of strike - slip faults: examples from the San Andreas Fault, California, J Geophys Res 94(B8):10204-10216. https://doi.org/10.1029/JB094iB08p10204

Belardinelli ME, Cocco M, Coutant O, Cotton F (1999) Redistribution of dynamic stress during coseismic ruptures: evidence for fault interaction and earthquake triggering. J Geophys Res 104 (B7):14925.

Bohnhoff M, Grosser H, Dresen G (2006) Strain partitioning and stress rotation at the North Anatolian fault zone from aftershock focal mechanisms of the 1999 Izmit M_W = 7.4 earthquake. Geophys J Int 166(1):373-385. https://doi.org/10.1111/j.1365-246X.2006.03027.x

Cundall PA (1971) A computer model for simulating progressive large scale movements in blocky rock systems. In: proceedings of the symposium of International Society of Rock Mechanics, vol. 1, Nancy: France Paper No II-8

Cundall PA, Strack ODL (1979) A discrete numerical model for granular assemblies. Géotechnique 29(1):47-65. https://doi.org/10.1680/geot.1979.29.1.47

Chi SL, Chi Y, Deng T, Liao CW, Tang XL, Chi L (2009) The necessity of building national strain-observation network from the strain abnormality before Wenchuan earthquake. Recent Dev World Seismol (1):1-13

Choi JH , Jin K , Enkhbayar D et al. (2012) Rupture propagation inferred from damage patterns, slip distribution, and segmentation of the 1957 M_W 8.1 Gobi-Altay earthquake rupture along the Bogd fault, Mongolia. J Geophys Res 117 (B12).

Ekström G, Nettles M, Dziewoński A (2012) The global CMT project 2004–2010: centroid-moment tensors for 13,017 earthquakes. Phys Earth Planet Inter 200-201:1-9. https://doi.org/10.1016/j.pepi.2012.04.002

Fälth B, Hökmark H, Lund B, Mai PM, Roberts R, Munier R (2015) Simulating earthquake rupture and off-fault fracture response: application to the safety assessment of the Swedish nuclear waste repository. B Seismol Soc Am 105(1):134-151. https://doi.org/10.1785/0120140090

Fuchs K, Muller B (2001) World Stress Map of the Earth: a key to tectonic processes and technological applications. Naturwissenschaften 88(9):357-371. https://doi.org/10.1007/s001140100253

Gutenberg B, Richter CF (1956) Magnitude and energy of earthquakes. Ann Geofis 9:1-15

Hauksson E (1994) State of stress from focal mechanisms before and after the 1992 Landers earthquake sequence. Bull Seismol Soc Am 84 (3): 917-934. https://doi.org/10.1016/0148-9062(95)94483-4

Hardebeck JL, Hauksson E (2001) Crustal stress field in southern California and its implications for fault mechanics. J Geophys Res 106 (B10): 21859-21882. https://doi.org/10.1029/2001jb000292

Hazzard JF, Young RP, Oates SJ (2002) Numerical modeling of seismicity induced by fluid injection in a fractured reservoir. In: proceedings of the 5th north American rock mechanics symposium, Mining and Tunnel Innovation and Opportunity, Toronto, Canada, 7–10 July 2002, pp 1023–1030

Hardebeck JL (2004) Stress triggering and earthquake probability estimates. J Geophys Res 109 (B04310):1-16

Harris, RA (1998) Introduction to Special Section: Stress Triggers, Stress Shadows, and Implications for Seismic Hazard. J Geophys Res 103(B10):24347-24358

Hofmann H, Babadagli T, Yoon JS, Blöcher G, Zimmermann G (2016a) A hybrid discrete/finite element modeling study of complex hydraulic fracture developments for enhanced geothermal systems (EGS) in granitic basements. Geothermics 64:362-381. https://doi.org/10.1016/j.geothermics.2016.06.016

Hofmann H, Babadagli T, Yoon JS, Zimmermann G (2016b) Multi-branched growth of fractures in shales for effective reservoir contact: a particle based distinct element modeling study. J Nat Gas Sci Eng 35:509-521. https://doi.org/10.1016/j.jngse.2016.09.004

Hu XP, Zang A, Heidbach O, Cui XF, Xie FR, Chen JW (2017) Crustal stress pattern in China and its adjacent areas. J Asian Earth Sci 149:20-28. https://doi.org/10.1016/j.jseaes.2017.07.005

Hardebeck JL, Okada T (2018) Temporal stress changes caused by earthquakes: a review. J Geophys Res 123:1350-1365. https://doi.org/10.1002/2017JB014617

Ivars DM, Pierce ME, Darcel C et al. (2011) The synthetic rock mass approach for jointed rock mass modelling. Int J Rock Mech Min Sci 48(2):219-244. https ://doi.org/10.1016/j.ijrmm s.2010.11.014

Itasca CGI (2008) PFC2D (particle flow code in 2 dimensions). Version 4.0. Itasca Consulting Group Inc. (ICG), Minneapolis, Minn

Kerkela S, Stock JM (1996) Compression directions north of the San Fernando valley determined from borehole breakouts. Geophys Res Lett 23 (23): 3365-3368. https://doi.org/10.1029/96GL03054

Kilb D, Gomberg J, Bodin P (2000) Triggering of earthquake aftershocks by dynamic stresses. Nature 408(6812):570-574

Lin W, Yeh EC, Ito H, Hung JH, Hirono T, Soh W, Ma KF, Kinoshita M, Wang CY, Song SR (2007) Current stress state and principal stress rotations in the vicinity of the Chelungpu fault induced by the 1999 Chi-Chi, Taiwan, earthquake. Geophys Res Lett 34(16):149-154. https://doi.org/10.1029/2007GL030515

Lin A, Jia D, Rao G, Yan B, Wu X, Ren Z (2011a) Recurrent morphogenic earthquakes in the past millennium along the strike-slip yushu fault, central Tibetan Plateau. Bull Seismol Soc Am 101 (6): 2755-2764. https://doi.org/10.1785/0120100274

Lin A, Rao G, Jia D, Xiaojun Wu, Yan B, Ren Z (2011b) Co-seismic strike-slip surface rupture and displacement produced by the 2010 Mw 6.9 Yushu earthquake, China, and implications for Tibetan tectonics. J Geodyn 52(3-4):249-259. https://doi.org/10.1016/j.jog.2011.01.001

Manighetti I, Campillo M, Sammis C, Mai P, King G (2005) Evidence for self-similar, triangular slip distributions on earthquakes: implications for earthquake and fault mechanics. J Geophys Res 110 (B05302):1-28. https://doi.org/10.1029/2004JB003174

Manighetti I, Campillo M, Bouley S, Cotton F (2007) Earthquake scaling, fault segmentation, and structural maturity. Earth Planet Sci Lett 253(3-4):429-438. https://doi.org/10.1016/j.epsl.2006.11.004

Manighetti I, Zigone D, Campillo M, Cotton F (2009) Self-similarity of the largest-scale segmentation of the faults: implications for earthquake behavior. Earth Planet Sci Lett 288(3-4):370-381. https://doi.org/10.1016/j.epsl.2009.09.040

Okada Y (1992) Internal deformation due to shear and tensile faults in a half-space. Bull Seismol Soc Am 82(2):1018-1040

Paillet FL, Kim K (1987) Character and distribution of borehole breakouts and their relationship to in situ stresses in deep Columbia River basalts. J Geophys Res 92(B7):6223-6234. https://doi.org/10.1029/JB092iB07p06223

Potyondy DO, Cundall PA (2004) A bonded-particle model for rock. Int J Rock Mech Min Sci 41(8):1329-1364. https://doi.org/10.1016/j.ijrmms.2004.09.011

Qiu ZH, Shi YL (2004) Application of observed strain steps to the study of remote earthquake stress triggering. Acta Seismol Sin 17(5): 534-541. https://doi.org/10.1007/s11589-004-0035-z

Qiu ZH, Ma J, Chi SL, Liu HM (2007) Earth's free torsional oscillations of the great Sumatra earthquake observed with borehole shear strainmeter. Chinese J Geophys 50(3):797-805

Qiu ZH, Zhang BH, Chi SL, Tang L, Song M (2011) Abnormal strain changes observed at Guza before the Wenchuan earthquake. Sci. China-Earth Sci 54(2):233-240. https://doi.org/10.1007/s11430-010-4057-1

Qiu ZH, Tang L, Zhang BH, Guo YP (2013) In situ calibration of and algorithm for strain monitoring using four-gauge borehole strainmeters (FGBS). J Geophys Res 118(4):1609-1618. https://doi.org/10.1002/jgrb.50112

Reasenberg PA, Simpson RW (1992) Response of regional seismicity to the static stress change produced by the loma prieta earthquake. Science 255(5052):1687-1690. https://doi.org/10.1126/science.255.5052.1687

Ratchkovski NA (2003) Change in stress directions along the central Denali fault, Alaska after the 2002 earthquake sequence. Geophys Res Lett 30(19):SDE15-1-SDE15-4. https://doi.org/10.1029/2003GL017905

Sbar ML, Engelder T, Plumb R, Marshak S (1979) Stress pattern near the San Andreas Fault, Palmdale, California, from near-surface in situ measurements. J Geophys Res 84 (NB1):156-164. https://doi.org/10.1029/JB084iB01p00156

Saucier F, Humphreys E, Weldon R (1992) Stress near geometrically complex strike-slip faults: application to the San Andreas Fault at Cajon Pass, Southern California. J Geophys Res 97(B4):5081-5094. https://doi.org/10.1029/91JB02644

Shamir G, Zoback MD (1992) Stress orientation profile to 3.5 km depth near the San Andreas Fault at Cajon Pass, California. J Geophys Res 97(B4):5059-5080. https://doi.org/10.1029/91JB02959

Stein RS (2000) The role of stress transfer in earthquake occurrence. Nature 402(6762):605-609. https://doi.org/10.1038/45144

Stein RS, Barka AA, Dieterich JH (2010) Progressive failure on the North Anatolian fault since 1939 by earthquake stress triggering. Geophys J Int (3):594-604.

Shifeng W, Erchie W, Xiaomin F, Bihong F (2008) Late Cenozoic systematic left-lateral stream deflections along the Ganzi-Yushu fault, Xianshuihe fault system, Eastern Tibet. Int Geol Rev 50(7):624-635. https://doi.org/10.2747/0020-6814.50.7.624

Stephansson O, Zang A (2012) ISRM suggested methods for rock stress estimation—part 5: establishing a model for the in situ stress at a given site.

Rock Mech Rock Eng 45(6):955-969. https://doi.org/10.1007/978-3-319-07713-0

Tobita M, Nishimura T, Kobayashi T, Hao KX, Shindo Y (2011) Estimation of coseismic deformation and a fault model of the 2010 Yushu earthquake using PALSAR interferometry data. Earth Planet Sci Lett 307(3-4):430-438. https://doi.org/10.1016/j.epsl.2011.05.017

Vermilye JM, Scholz CH (1998) The process zone: A microstructural view of fault growth. J Geophys Res 103 (B6).

Vermilye JM, Scholz CH (1999) Fault propagation and segmentation: insight from the microstructural examination of a small fault. J Struct Geol 21(11): 1623-1636.

Wang Q, Zhang PZ, Freymueller JT, Bilham R, Larson KM, Lai X, You X, Niu Z, Wu J, Li Y, Liu J, Yang Z, Chen Q (2001) Present-day crustal deformation in China constrained by global positioning system measurements. Science 294(5542):574-577. https://doi.org/10.1126/science.1063647

Wen X, Xu X, Zheng R, Xie Y, Wan C (2003) Average slip-rate and recent large earthquake ruptures along the Garzê-Yushu fault. Science in China Series D: Earth Sciences 46:276-288. https://doi.org/10.1360/03dz0022

Xu H, Arson C (2015) Mechanistic analysis of rock damage anisotropy and rotation around circular cavities. Rock Mech Rock Eng 48(6):2283-2299. https://doi.org/10.1007/s00603-014-0707-5

Yin ZM, Rogers GC (1995) Rotation of the principal stress directions due to earthquake faulting and its seismological implications. Bull Seismol Soc Am 85 (5):1513-1517. https://doi.org/10.1029/95JB01688

Yang SX (2013) Study on the Distribution Characteristics of Crustal Stress Field in Chinese Mainland. Dissertation, Beijing jiaotong University

Yoon JS, Stephansson O, Min K (2014a) Relation between earthquake magnitude, fracture length and fracture shear displacement in the KBS-3 repository at Forsmark - Main Review Phase.

Yoon JS, Zang A, Stephansson O (2014b) Numerical investigation on optimized stimulation of intact and naturally fractured deep geothermal reservoirs using hydro-mechanical coupled discrete particles joints model. Geothermics 52:165-184. https://doi.org/10.1016/j.geothermics.2014.01.009

Yoon JS, Zimmermann G, Zang A (2015a) Numerical Investigation on Stress Shadowing in Fluid Injection-Induced Fracture Propagation in Naturally Fractured Geothermal Reservoirs. Rock Mech Rock Eng 48(4):1439-1454. https://doi.org/10.1007/s00603-014-0695-5

Yoon JS, Zimmermann G, Zang A (2015b) Discrete element modeling of fluid injection-induced seismicity and activation of nearby fault. Can

Geotech J 52(10):1457-1465. https://doi.org/10.1139/cgj-2014-0435

Yoon JS, Stephansson O, Min KB (2016) Modelling of the thermal evolution of the KBS-3 repository at Forsmark and associated induced seismic activity. SSM Technical Note 2016:23, Swedish Radiation Safety Authority

Yoon JS, Stephansson O, Zang A, Min KB, Lanaro F (2017) Discrete bonded particle modelling of fault activation near a nuclear waste repository site and comparison to static rupture earthquake scaling laws. Int J Rock Mech Min Sci 98:1-9. https://doi.org/10.1016/j.ijrmms.2017.07.008

Yoon JS, Zang A (2019) 3D Thermo-mechanical coupled modelling of thermo-seismic response of a fractured rock mass related to the final disposal of spent nuclear fuel and nuclear waste in hard rock. SSM Research Report 2019:15, Swedish Radiation Safety Authority

Yoshida K, Hasegawa A, Saito T, Asano Y, Tanaka S, Sawazaki K, Urata Y, Fukuyama E (2016) Stress rotations due to the M6. 5 foreshock and M7. 3 main shock in the 2016 Kumamoto, SW Japan, earthquake sequence. Geophys Res Lett 43(19): 10097-010104.

Yu Z, Zhao D, Li J, Huang Z, Nishizono Y, Inakura H (2019) Stress Field in the 2016 Kumamoto Earthquake (M 7.3) Area. J Geophys Res 124: 2638-2652.

Zoback MD, Zoback ML, Van Mount S, Suppe J, Eaton JP, Healy JH, Oppenheimer D, Reasenberg P, Jones L, Raleigh CB, Wong IG, Scotti O, Wentworth C (1987) New evidence on the state of stress of the san andreas fault system. Science 238(4830):1105-1111. https://doi.org/10.1126/science.238.4830.1105

Zhang YZ, Dusseault MB, Yassir NA (1994) Effects of rock anisotropy and heterogeneity on stress distributions at selected sites in North America. Eng Geol 37(3):181-197. http://377.rm.cglhub.com/10.1016/0013-7952(94)90055-8

Zhao DP, Kanamori H, Wiens D (1997) State of stress before and after the 1994 Northridge earthquake. Geophys Res Lett 24 (5):519-522. https://doi.org/10.1029/97GL00258

Zang A, Stephansson O (2010) Stress field of the earth's crust. Springer, Netherlands, Dordrecht. https://doi.org/ 10.1007/978-1-4020-8444-7

Zhao X, Young RP (2011) Numerical modeling of seismicity induced by fluid injection in naturally fractured reservoirs. Geophysics 76 (6): WC167-WC180. https://doi.org/10.1190/GEO2011-0025.1

Zang A, Yoon JS, Stephansson O, Heidbach O (2013) Fatigue hydraulic fracturing by cyclic reservoir treatment enhances permeability and reduces induced seismicity. Geophys J Int 195(2): 1282-1287. https://doi.org/10.1093/gji/ggt301

Zhou J, Zhang L, Braun A, Han Z (2016) Numerical modeling and investigation of fluid-driven fracture propagation in reservoirs based on a modified fluid-mechanically coupled model in two-dimensional particle flow code. Energies 9(9):699: 1-19. https://doi.org/10.3390/en9090699

Zheng G, Wang HJ, Wright. T, Lou Y, Zhang R, Zhang W, Shi C, Huang J, Wei N (2017) Crustal deformation in the India-Eurasia collision zone from 25 years of GPS measurements: crustal deformation in Asia from GPS. J Geophys Res 122(11):9290-9312. https://doi.org/10.1002/2017JB014465

Zhou J, Zhang L, Braun A, Han Z (2017) Investigation of processes of interaction between hydraulic and natural fractures by PFC modeling comparing against laboratory experiments and analytical models. Energies 10(7):1001. https://doi.org/10.3390/en10071001

Zhang L, Zhou J, Braun A, Han Z (2018) Sensitivity analysis on the interaction between hydraulic and natural fractures based on an explicitly coupled hydro-geomechanical model in PFC2D. J Petrol Sci Eng 167:638-653. https://doi.org/10.1016/j.petrol.2018.04.046

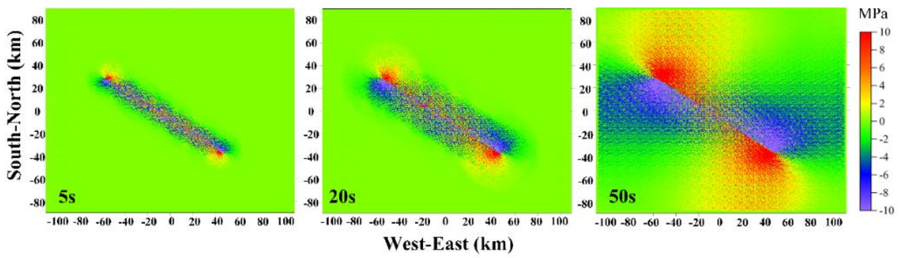

Fig. S1 Spatiotemporal evolution of compression (red) and dilatation (blue) stress quadrants for the LE scenario.

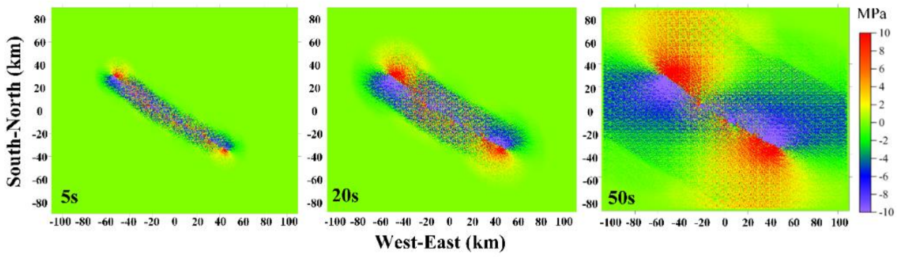

Fig. S2 Spatiotemporal evolution of compression (red) and dilatation (blue) stress quadrants for the CE scenario.

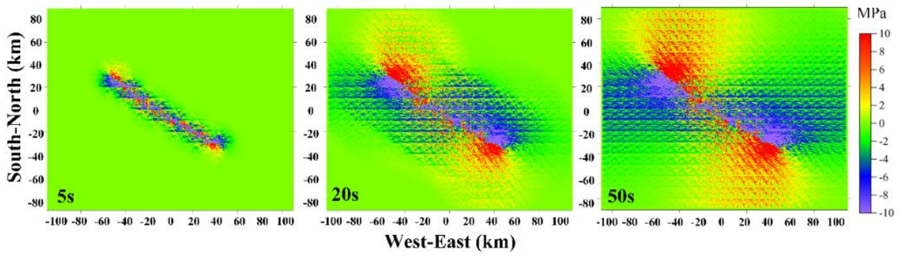

Fig. S3 Spatiotemporal evolution of compression (red) and dilatation (blue) stress quadrants for the CEP scenario.